Supporting Information:

Understanding the Role of Non-Fullerene Acceptor Crystallinity on the Charge Transport Properties and Performance of Organic Solar Cells

Pierluigi Mondelli,[*a,d] Pascal Kaienburg,[a] Francesco Silvestri,[b] Rebecca Scatena,[a] Claire Welton,[c] Martine Grandjean,[d] Vincent Lemaur,[e] Eduardo Solano,[f] Mathias Nyman,[g] Peter N. Horton,[h] Simon J. Coles,[h] Esther Barrena,[b] Moritz Riede,[a] Paolo Radaelli,[a] David Beljonne,[e] G. N. Manjunatha Reddy[c] and Graham Morse[d]

[a] Clarendon Laboratory, University of Oxford, Parks Road, Oxford, OX1 3PU, United Kingdom. E-mail: pierluigi.mondelli@gmail.com

[b] Institut de Ciència de Materials de Barcelona, ICMAB-CSIC, Campus UAB, 08193 Bellaterra, Spain

[c] University of Lille, CNRS, Centrale Lille, Univ. Artois, UMR 8181- UCCS - Unité de Catalyse et Chimie du Solide, F-59000 Lille, France

[d] Merck Chemicals Ltd, Chilworth Technical Centre, University Parkway, Southampton, SO16 7QD, United Kingdom

[e] Laboratory for Chemistry of Novel Materials, University of Mons, Place du Parc, 20, 7000 Mons (Belgium)

[f] ALBA Synchrotron Light Source, NCD-SWEET beamline, Cerdanyola del Vallès, 08290 Spain

[g] Physics, Faculty of Science and Engineering, Åbo Akademi University, 20500 Turku, Finland

[h] EPSRC Crystallographic Service, Department of Chemistry, University of Southampton, Highfield, SO17 1BJ, UK

Table of Contents

1. Solid-state NMR analysis of o-IDTBR powder	**2-5**
2. Powder and Single Crystal X-Ray Diffraction	**6-8**
3. Film Morphology by 2D-GIWAXS and AFM	**9-19**
4. AFM Watershed Analysis	**20-25**
5. Electron Mobility by MIS-CELIV	**26-27**
6. Annealing Temperature, Dark J-V and β_{exp}	**27**
7. References	**28**

1. Solid-state NMR analysis of o-IDTBR powder

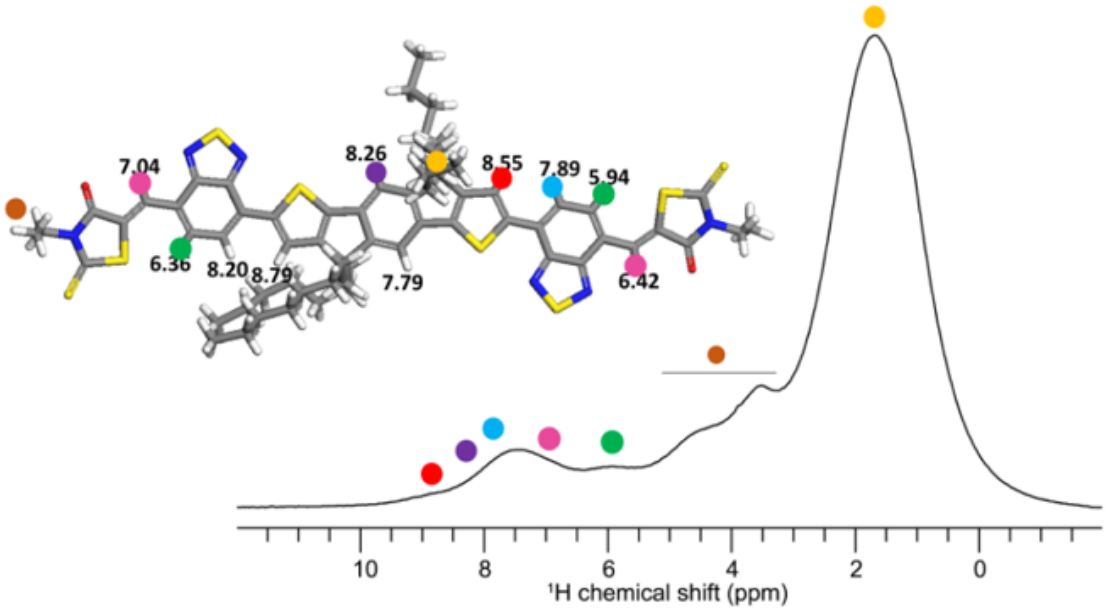

Figure S1. 1D solid-state ^{1}H NMR spectrum of o-IDTBR powder acquired at 18.8 T (^{1}H = 800 MHz) with 50 kHz MAS. Peak assignments are colour coded as depicted in the crystal structure shown in the inset.

Figure S1 presents ^{1}H MAS NMR spectra of O-IDTBR powder, whereby the ^{1}H peaks are color coded as depicted in the schematic structure figure of O-IDTBR shown on top and the isotropic chemical shifts calculated by GIPAW-DFT approach are overlaid. The broad ^{1}H peak centered at ~1.7 ppm is due to the branched alkyls sidechains attached to the aromatic core. The different distributions of ^{1}H peaks in the 3-5 ppm range are due to the -NCH_2CH_3 moieties attached to the terminal 3-ethyl-2-thioxothiazolidin-4-one groups. In the aromatic region, the peak at ~6 ppm is due to the protons in the benzothiadiazole (BDT) groups (green dots), and the low ppm chemical shift value of these BDT protons can be ascribed to the ring current effects caused by the partial overlap of the aromatic rings. The peak at ~7 ppm can be attributed to the -CH moieties bridging the BDT and 3-ethyl-2-thioxothiazolidin-4-one groups as depicted in the magenta dot. The overlapped peaks in the range between 7.5 to 8.5 ppm are due to the protons in the BDT groups facing towards thiophene (T) groups (blue dot) and the protons in the central benzene ring (purple dots). The weak intensity peak at ~8.8 ppm is due to thiophene protons (red dot).

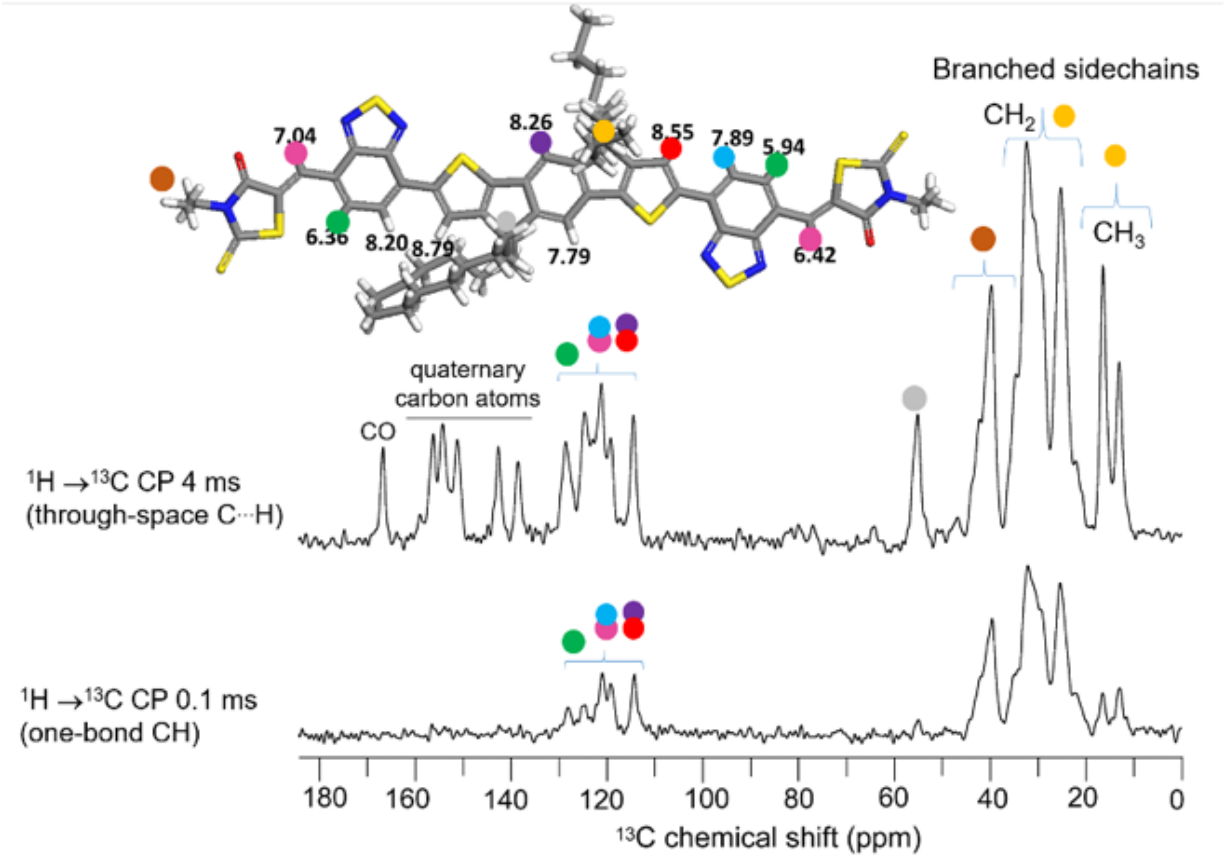

Figure S2. 1D solid-state $^{13}C^{1}$ CP-MAS NMR spectra of o-IDTBR powder acquired with 0.1 (bottom) and 3 ms (top) CP contact time. All spectra were acquired at 18.8 T and 50 kHz MAS. Peak assignments are colour coded as depicted in the crystal structure shown in the inset.

For O-IDTBR powder, the $^{1}H \rightarrow ^{13}C$ cross-polarization (CP)-MAS NMR spectra of o-IDTBR were acquired with 0.1 ms and 3 ms of CP contact time and compared. CP-MAS based experiments exploit the enhancement of the ^{13}C signal intensities that are increased by transfer of ^{1}H spin-polarization by the adjacent protons, according to the strengths of the ^{1}H-^{13}C dipole-dipole couplings. The isotropic ^{13}C chemical shifts are color coded as presented in the spectrum, the CH_3 peaks are well resolved in 10-20 ppm range and the CH_2 moieties produce peaks in 20-37 ppm range. The peaks around 40 ppm are due to the -NCH_2CH_3 groups of 3-ethyl-2-thioxothiazolidin-4-one, and the peak centered at ~55 ppm can be assigned to the quaternary carbon atom bearing the branched alkyl sidechains. In the aromatic region, the one-bond CH moieties produce peaks in the 110-130 ppm; the broad peak in the 110-115 range originates from the protonated carbon atoms in the benzene ring that produces a peak at ~112 ppm (purple dot) and the protonated thiophene carbon atoms that give rise to a peak at ~ 115 ppm (red dot). Partially resolved peaks in the 118-122 ppm range are due to the protonated carbon atom (facing towards the T group as depicted by the blue dot) and the -CH moieties (purple dots) bridging the BDT and 3-ethyl-2-thioxothiazolidin-4-one groups. By comparison, a CP-MAS NMR spectrum of o-IDTBR was acquired with 3 ms CP contact time which displayed additional peaks corresponding to the quaternary carbon atoms (top spectrum), signals of which are enhanced by the CP transfer via through-space ^{13}C-^{1}H dipolar interactions. Specifically, the ^{13}C peak of the quaternary carbon atom bearing the sidechains (gray dot) is enhanced as shown by the peak at ~55 ppm. In addition, the ^{13}C signals associated with the quaternary aromatic carbon atoms at 135-160 ppm are enhanced by the CP transfer from the adjacent protons via ^{13}C-^{1}H dipolar couplings. The ^{13}C peak at ~168 is due to the carbonyl group of the O-IDTBR molecules.

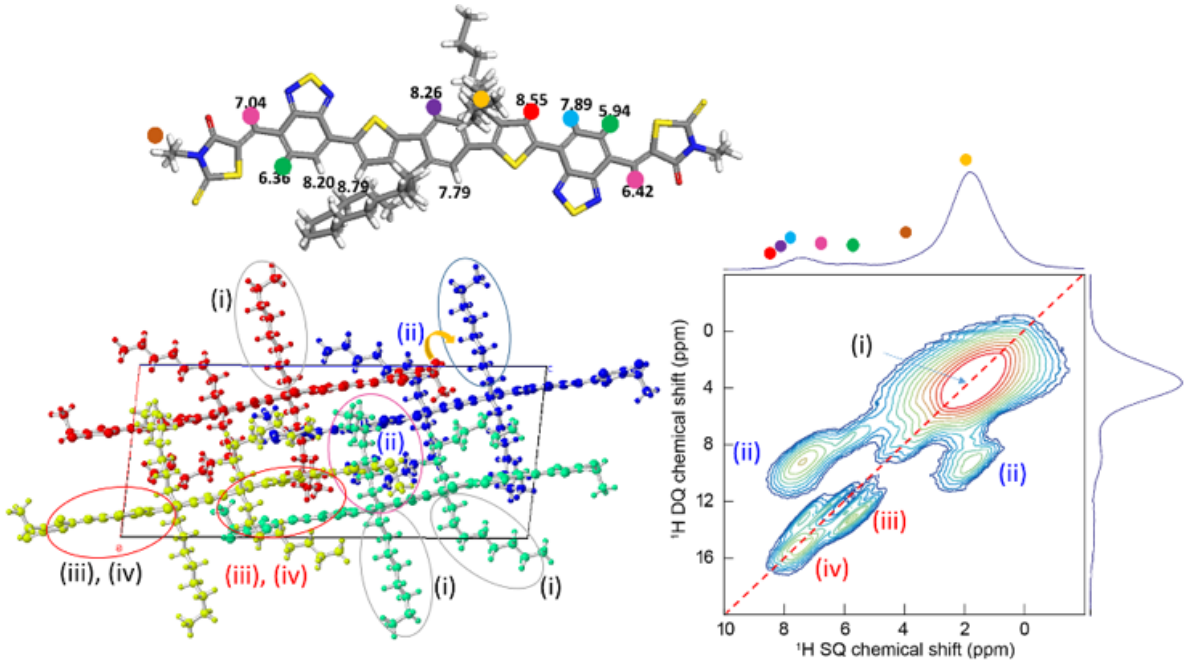

Figure S3. 2D solid-state ^{1}H-^{1}H NMR spectrum of o-IDTBR powder acquired at 18.8 T (^{1}H = 800 MHz) with 50 kHz MAS. Peak assignments are colour coded as depicted in the crystal structure shown in the inset. ^{1}H chemical shift values associated with the aromatic protons are depicted in the GIPAW-DFT geometry optimized structure as shown by the coloured dots.

2D ^{1}H-^{1}H double-quantum single-quantum (DQ-SQ) correlation spectrum presented in **Figure S3** displays the DQ peaks in the vertical axis that correspond to ^{1}H-^{1}H proximities in less than 5 Å distance. The ^{1}H SQ signals are color coded as depicted in the schematic structure figure of O-IDTBR shown on top. In particular, the different aromatic chemical shifts of thiophene (T) and benzothiadiazole (BDT) are due to the different aromatic ring current effects. The inter- and intramolecular ^{1}H-^{1}H proximities in the alkyl and aromatic regions (i, ii, iii, and iv) that contribute to the ^{1}H DQ peaks are marked by ovals in the crystal structure in the left. The broad DQ peak at ~3.6 ppm (i) is due to the inter-and intramolecular ^{1}H-^{1}H proximities in branched sidechains. The DQ peaks at ~7.7 and ~9.4 ppm (ii) are due to the dipolar coupled ^{1}H-^{1}H pairs between branched sidechains and aromatic groups (T and BDT). The DQ peaks in the aromatic region (iii and iv) are due to the intramolecular ^{1}H-^{1}H proximities between the aromatic moieties, whereby the DQ peak 12.1 ppm is attributable to intramolecular ^{1}H-^{1}H dipolar interactions between the BDT proton and C-H protons in the bridged position (green and magenta dots).The DQ peak at 13.1 ppm is due to the intramolecular ^{1}H-^{1}H dipolar interactions between the BDT protons (blue and green dots), and the peak at 15.2 ppm is ascribed to the intramolecular ^{1}H-^{1}H dipolar interactions between the BDT and T protons (blue and red dots) of O-IDTBR molecules. The different packing interactions that contribute to the DQ peaks are marked by ovals in the crystal structure depicted in the left.

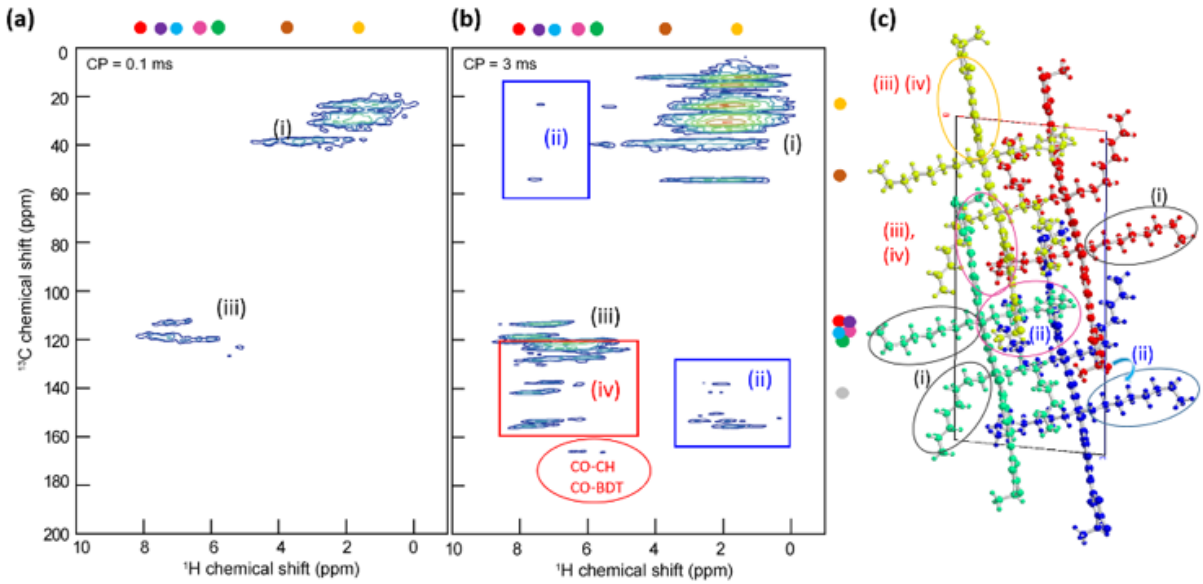

Figure S4. 2D solid-state ^{1}H-^{13}C heteronuclear correlation (HETCOR) spectrum of o-IDTBR powder acquired with (a) 0.1 ms and (b) 3 ms CP contact time. Peak assignments are color coded as depicted in the crystal structure shown in (c). All spectra were acquired at 18.8 T (^{1}H = 800 MHz) with 50 kHz MAS.

Figure S4 presents 2D HETCOR spectra acquired with 0.1 ms and 3 ms CP contact times in order to detect 2D peaks that originate from directly bonded C-H as well as through-space dipolar coupled C···H moieties in o-IDTBR molecules. Inter- and intramolecular C-H proximities corresponding to the 2D peaks are shown in the crystal structure (c). In the spectrum acquired with 0.1 ms CP contact time, the isotropic ^{13}C chemical shifts at $\delta(^{13}C)$ = 10-45 ppm are due to the directly bonded C-H moieties in alkyl groups (yellow dots), and the isotropic ^{13}C chemical shifts at $\delta(^{13}C)$ = 110-122 ppm are due to the directly bonded C-H moieties in BDT (blue and green dots), T (red dot), CH moiety at the bridged position (magenta) and benzene ring (purple dots) at the aromatic core. In addition to these, the 2D HETCOR spectrum acquired with 3 ms CP contact time exhibits the 2D peaks corresponds to the through-space inter and intramolecular ^{1}H-^{13}C dipolar interactions between aliphatic and aromatic groups, as depicted in the boxes and ovals. Specifically, the 2D ^{13}C-^{1}H correlation peaks associated with the quaternary carbon atoms that are in close proximities to aromatic protons in the core are emerged as depicted in the red color box. The 2D peaks shown in the blue boxes are due to the inter- and intramolecular ^{13}C-^{1}H dipolar interactions between the alkyl chains and the aromatic moieties. The carbonyl carbon atom is in close proximity to the CH protons (magenta) and intermolecularly with the BDT protons (green dots) that lead to the 2D peaks as depicted in the red oval.

2. Powder and Single Crystal X-Ray Diffraction

Manual calculation of the lattice parameters

The *o*-IDTBR lattice parameters (a, b and c) for powder sample were initially obtained by solving the reciprocal-space metric tensor for monoclinic structures:

$$\frac{1}{d^2} = \frac{1}{sin^2\beta}\left(\frac{h^2}{a^2} + \frac{k^2 sin^2\beta}{b^2} + \frac{l^2}{c^2} - \frac{2hlcos\beta}{ac}\right)$$

where the positions of the (0 1 1), (0 1 2) and (110) were derived from the experimental pattern. The unit cell angles (α, β and γ) were assumed to be the same as in single crystal. The results are shown in (Table S1) and compared to the single crystal unit cell and the ones obtained by Le Bail refinement of powder data.

Table S1. Evolution of the o-IDTBR unit cell parameters from the known single crystal data to the manual and Le Bail refinements.

Unit Cell	a (Å)	b (Å)	c (Å)	α (°)	β (°)	γ (°)	Volume (Å³)
Single crystal	13.7663(2)	15.81032(17)	32.7146(3)	90	96.2928(12)	90	7077.43(15)
Manual	14.0646	16.0432	32.7057	90	96.293	90	7335.288
Le Bail	14.03086	16.06125	32.68444	90	96.716	90	7314.994

Temperature effect on the single crystal unit cell

The effect of the temperature on the NFA unit cell parameters was explored by performing temperature-dependent single-crystal XRD on IDIC‡ (Figure S5, Table S2). The experiments have shown how temperature can influence both lattice parameters and angles of IDIC.

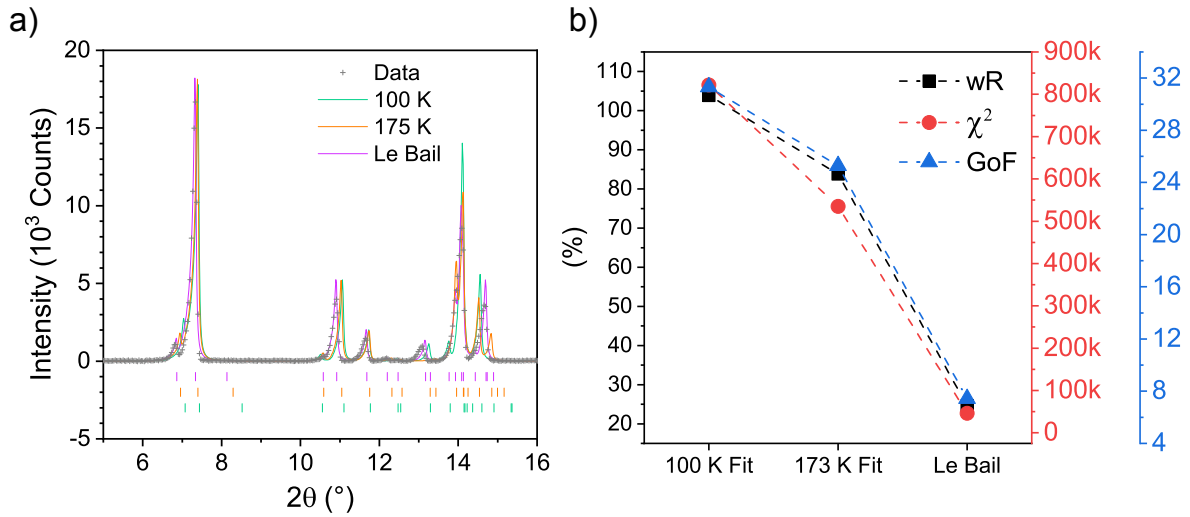

Figure S5 a) IDIC powder XRD datapoints with Le Bail refinement compared to the simulated powder pattern from the single crystals measured at 100 and 173 K. b) Fitting parameters evolution towards lower values

Table S2 IDIC unit cell parameters evolution with temperature

Structure	Crystal System	Space Group	a (Å)	b (Å)	c (Å)	α (°)	β (°)	γ (°)	Volume (Å³)
100 K	triclinic	$P\bar{1}$	8.6679(4)	12.5073(7)	13.5784(6)	72.096(4)	75.545(4)	88.839(4)	1353.88(12)
173 K	triclinic	$P\bar{1}$	8.6379(4)	12.6391(6)	13.9041(5)	70.650(4)	75.044(4)	88.148(4)	1381.35(11)
Le Bail	triclinic	$P\bar{1}$	8.63994	12.80154	14.39796	69.913	74.405	88.479	1436.737

‡ The IDIC single crystal structures are accessible from the CCDC Database: Deposition Number 2226731 for the measurement taken at 173 K and Deposition Number 2040188 for the dataset taken at 100 K.

Le Bail analysis

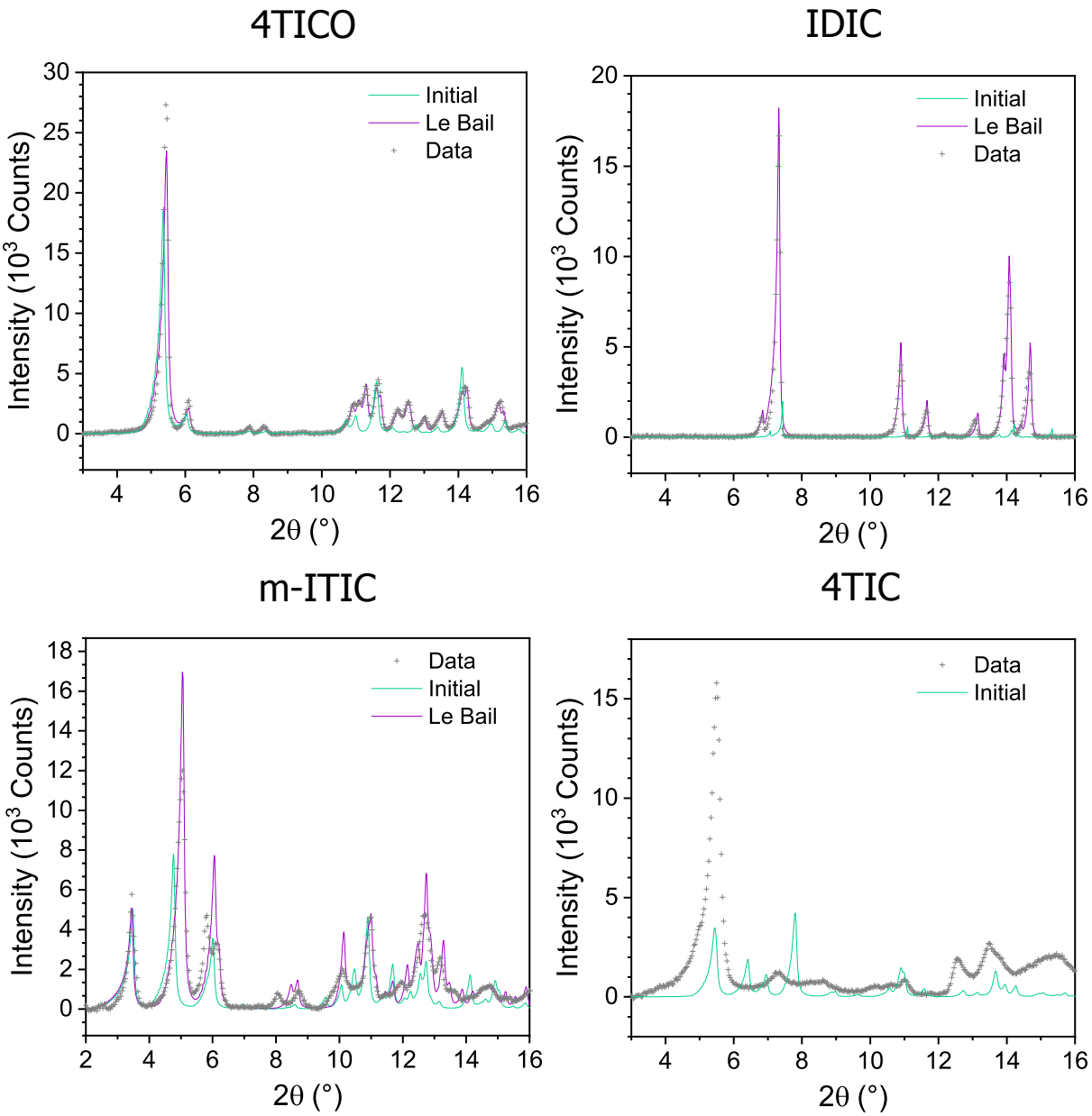

Figure S6. Powder XRD datapoints with Le Bail refinement compared to the simulated powder pattern from the single crystal.

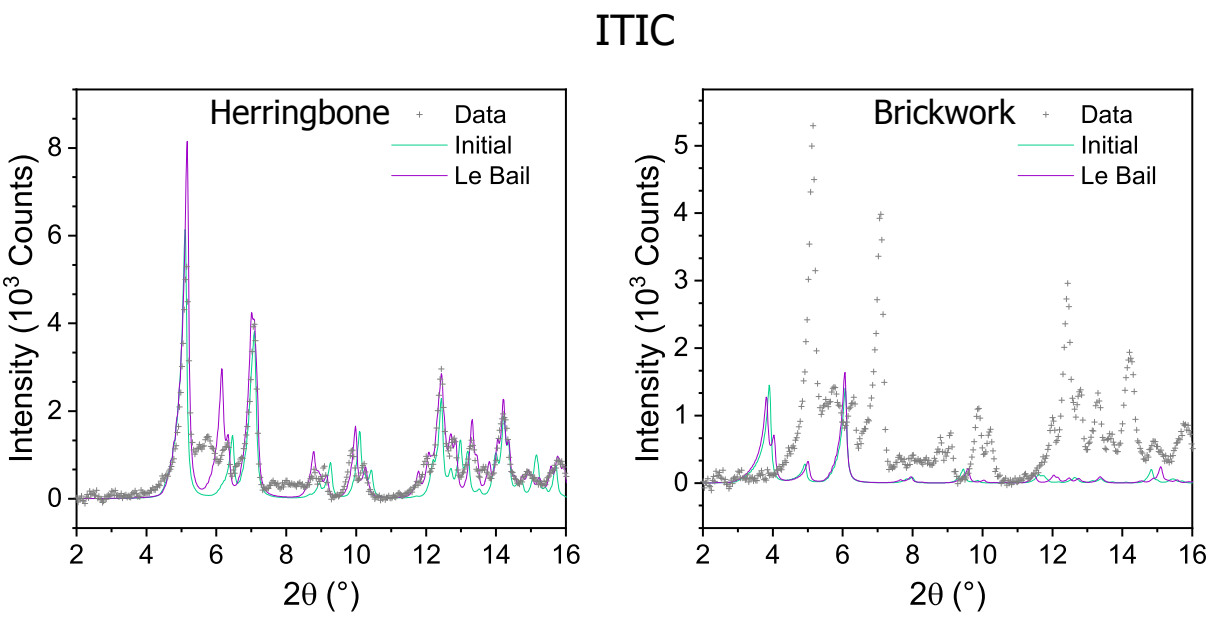

Figure S7. Powder XRD datapoints with Le Bail refinement compared to the simulated powder pattern from the single crystal.

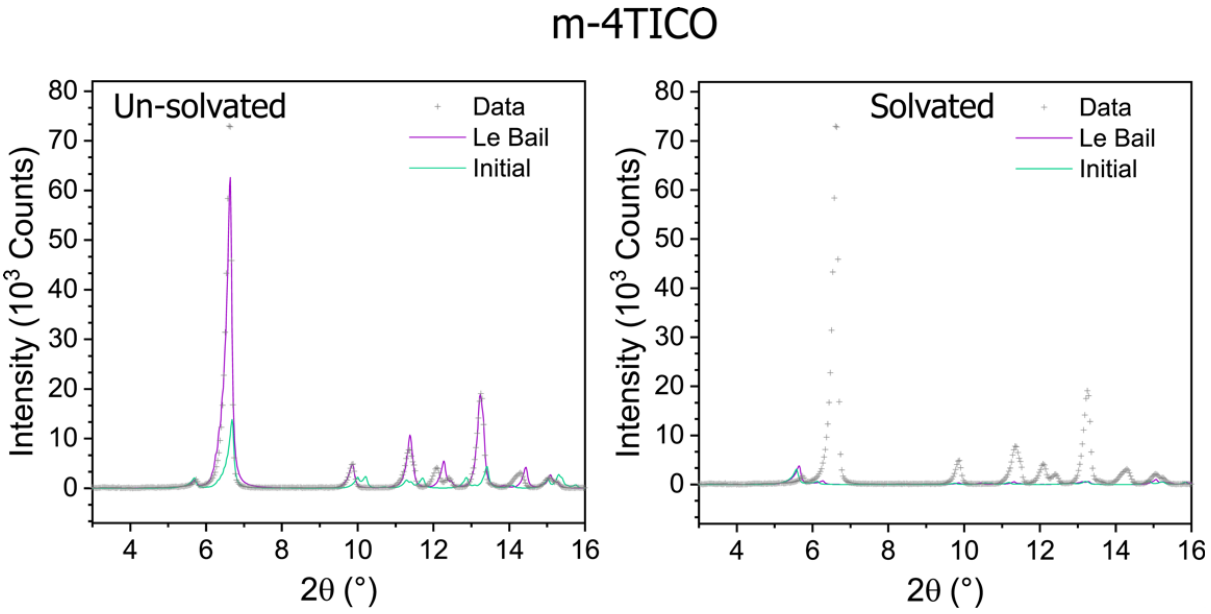

Figure S8. Powder XRD datapoints with Le Bail refinement compared to the simulated powder pattern from the single crystal.

Table S3 NFA unit cell parameters for the known crystal structures in comparison with the parameters obtained from Le Bail refinement.

CCDC	Molecule	Solvates	a (Å)	b (Å)	c (Å)	α (°)	β (°)	γ (°)	Volume (Å^3)	GOF	Chi^2	wR
Before Le Bail Refinement												
HEHQUJ01	ITIC	none	14.9009(7)	15.5043(4)	18.1199(5)	99.309(2)	101.541(3)	108.366(3)	3777.2(2)	10.43	91145.1	24.046
KIZSUK	ITIC	CH_2Br_2	8.420(6)	23.019(17)	23.126(17)	101.780(10)	95.319(10)	91.105(14)	4366(5)	18.24	278780.8	42.055
VUBJOU	*m*-ITIC	$CHCl_3$	8.7454(13)	18.872(2)	25.2647(18)	87.770(8)	88.724(9)	78.001(12)	4075.1(9)	20.51	352372	38.001
VUBJEK	4TICO	C_3H_6O	15.2836(2)	20.0101(5)	29.3242(6)	90	29.3242(6)	90	8968.1(3)	18.95	300794.4	37.892
FOSPOV	*o*-IDTBR	none	13.7663(2)	15.81032(17)	32.7146(3)	90	96.2928(12)	90	7077.43(15)	9.10	63293.5	31.079
VUBKAH	IDIC	none	8.6679(4)	12.5073(7)	13.5784(6)	72.096(4)	75.545(4)	88.839(4)	1353.88(12)	20.93	367143.8	69.427
2236094	*m*-4TICO	none	8.7845(7)	15.3726(13)	16.7896(13)	67.136(7)	85.678(7)	79.630(7)	2055.0(3)	35.82	1075472.2	62.264
VUBJIO	*m*-4TICO	$CHCl_3$	8.6526(3)	16.4878(8)	18.0435(8)	114.697(5)	103.822(4)	90.890(4)	2251.45(19)	40.43	1369716.7	70.267
YEBKEY	4TIC	C_7H_8, CH_3OH	13.969(7)	17.144(9)	17.970(10)	104.668(16)	109.998(17)	96.169(14)	3822.08	24.62	507853	44.652
After Le Bail Refinement												
HEHQUJ01	ITIC	none	15.06724	15.46733	17.89986	100.067	100.804	107.462	3788.083	7.87	51968.4	18.157
KIZSUK	ITIC	CH_2Br_2	8.57001	23.49976	22.22479	100.617	92.928	93.867	4380.067	18.16	274453.9	41.727
VUBJOU	*m*-ITIC	$CHCl_3$	8.74588	17.77874	25.48191	88.391	89.072	78.262	3877.599	10.96	1000667.7	20.331
VUBJEK	4TICO	C_3H_6O	15.66764	19.60675	29.04299	90	90.799	90	8920.893	5.65	26766	11.303
FOSPOV	*o*-IDTBR	none	14.03086	16.06125	32.78444	90	96.716	90	7337.375	5.02	19267.4	17.148
VUBKAH	IDIC	none	8.67925	12.79671	14.4997	70.019	74.42	88.239	1454.553	7.43	46096.4	24.6
N/A	*m*-4TICO	none	9.0868	15.7656	16.6819	67.74	85.699	79.53	2167.014	16.70	233612.4	29.019
VUBJIO	*m*-4TICO	$CHCl_3$	8.74656	16.15453	17.81585	114.163	104.908	89.942	2203.878	40.27	1348979.8	69.733

3. Film Morphology by 2D-GIWAXS and AFM

4TIC

4TIC 2D-GIWAXS pattern (Figure S6c) is in good agreement with the one obtained in our previous report.[2] We have simulated the 2D-GIWAXS map by using the single crystal unit cell available from literature[3] (Figure S9a) and oriented along the (1 0 0) direction. Such direction is parallel to the π-π stacking (4 -1 -1) and the lamellar (1 0 0) peak, which is representative of a face-on orientation of 4TIC domains with respect to the substrate (Figure S9b). Although the (1 0 0) lamellar contribution is not visible from the simulated data (all crystallites are assumed to be perfectly oriented along the (1 0 0) and therefore are not accessible[4]), experimental and simulated GIWAXS are in good agreement confirming a face-on 3D reticular packing with respect to the substrate. As the 4TIC lamellar feature is still evident from the PBTZT-stat-BDTT-8:4TIC GIWAXS (Figure S9d) and out-of-plane integration profile (Figure S6h), we assume that the NFA is maintaining its crystalline order in blend with a slightly relaxed (1 0 0) periodicity (Table S5) compared to the pure NFA film.

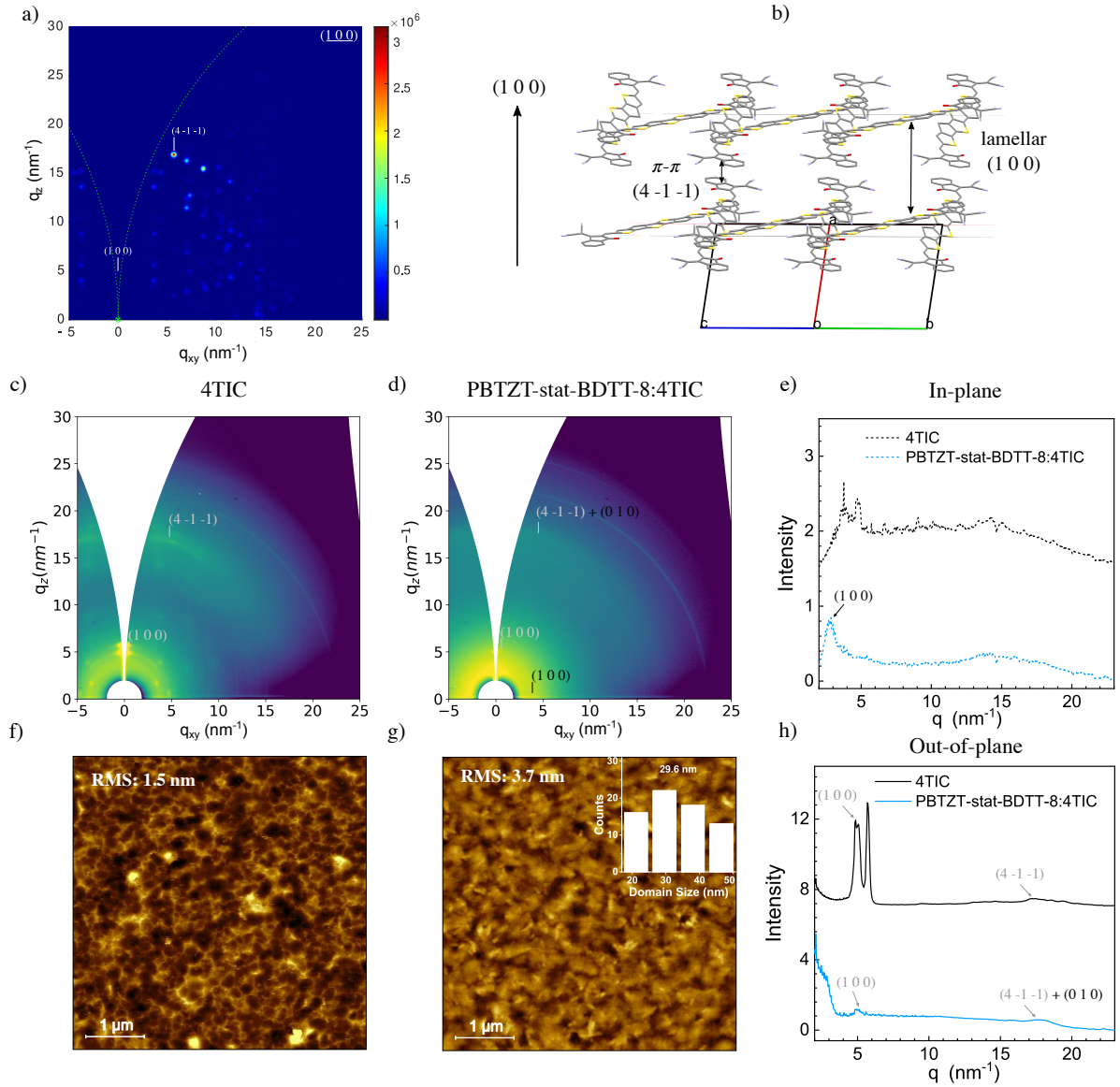

Figure S9. Simulated 2D-GIWAXS pattern of the 4TIC unit cell oriented along the (1 0 0) direction (a). Graphical representation of the π-π stacking (4 -1 -1) and lamellar (1 0 0) peaks orientation with respect to the (1 0 0) vector (b). 4TIC (c) and PBTZT-stat-BDTT-8:4TIC (d) GIWAXS pattern with in-plane (e) and out-of-plane (g) integration profiles. 5x5 µm AFM images of 4TIC (f) and PBTZT-stat-BDTT-8:4TIC (g) films with domain size distribution and average value (inset).

Table S4. Crystallographic information of the main peaks observed by 2D-GIWAXS on 4TIC and PBTZT-stat-BDTT-8:4TIC films. AFM domain size and domain purity are also shown.

Component	Peak	Orientation	q (nm^{-1})	d (nm)	FWHM (nm^{-1})	CCL (nm)	g	Domain Size (nm)	φ (%)
			NFA film						
4TIC	(1 0 0)	Out-of-plane	5.09	1.23	0.29	19.5	9.5	N/A	N/A
4TIC	(4 -1 -1)	Out-of-plane	17.34	0.36	1.16	4.9	10.3	-	-
			Blend film						
4TIC	(1 0 0)	Out-of-Plane	5.02	1.25	0.58	9.0	14.1	29.6	30.3
PBTZT-stat-BDTT-8	(1 0 0)	In-plane	2.75	2.28	0.87	6.5	22.4	-	-
PBTZT-stat-BDTT-8, 4TIC	(0 1 0) + (4 -1 -1)	Out-of-plane	17.81	0.35	3.00	1.9	16.4	-	-

***m*-4TICO**

m-4TICO 2D-GIWAXS pattern (Figure S10c) shows a strong Bragg peak along q_z and other less intense features in the q map. To verify whether the NFA arrangement in film is compatible to the phase existing in powder and single crystal, we have simulated the 2D-GIWAXS of the single crystal unit cell (Le Bail refined) and oriented along the (0 1 1) direction (Figure S10a). Such direction is parallel to the lamellar (1 0 0) peak and diagonal with respect to π-π stacking (2 3 2). This is representative of a *quasi*-edge-on orientation of the m-4TICO domains with respect to the substrate (Figure S10b). The good agreement between experimental and simulated GIWAXS confirms a *quasi*-edge-on 2D brickwork packing with respect to the substrate. As the m-4TICO lamellar feature is still evident from the PBTZT-stat-BDTT-8:m-4TICO GIWAXS (Figure S10d) and out-of-plane integration profile (Figure S10h), we assume that the NFA is maintaining its crystalline order in blend with a slightly relaxed (0 1 1) periodicity (Table S5) compared to the pure NFA film.

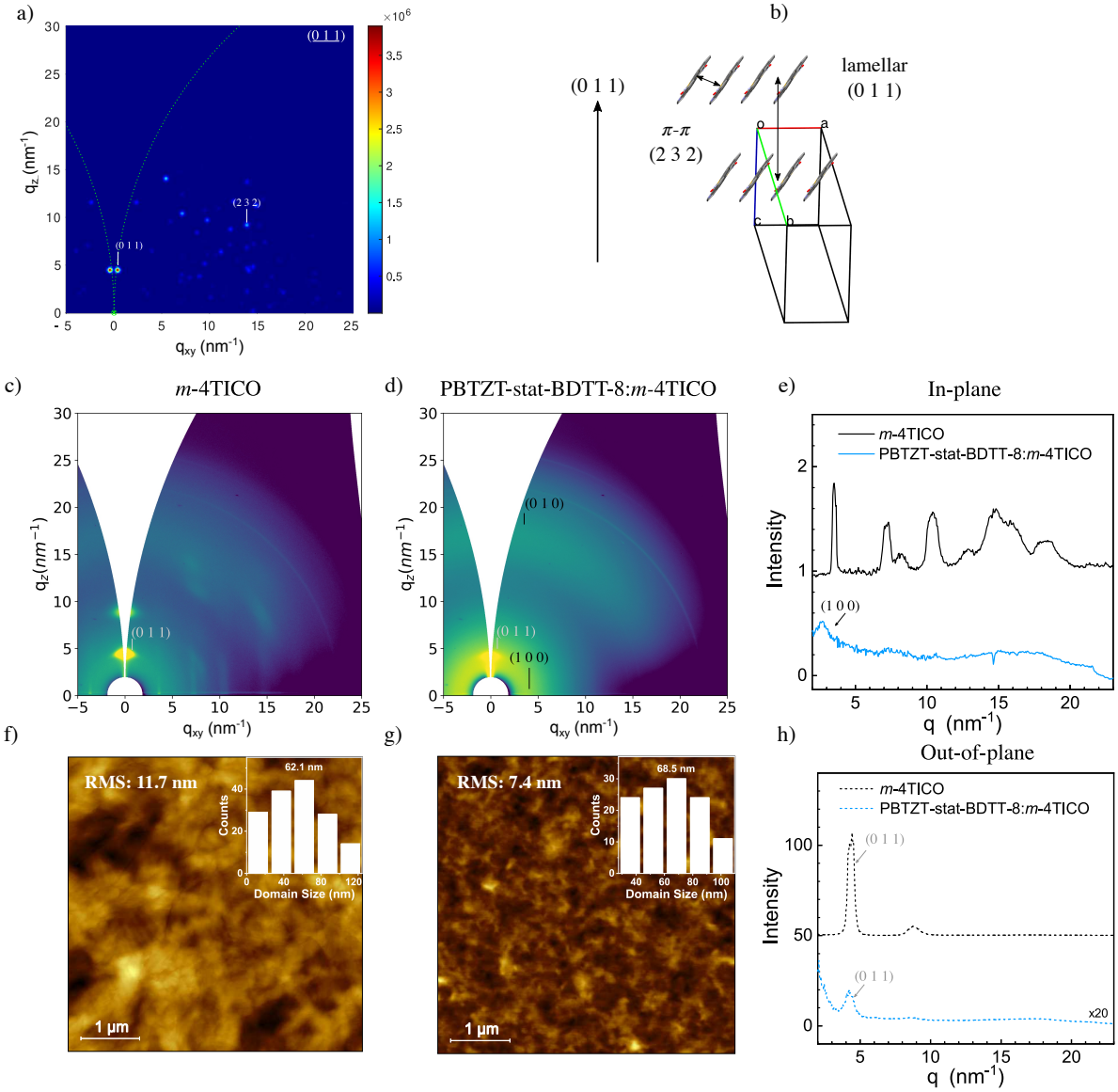

Figure S10. Simulated 2D-GIWAXS pattern of the m-4TICO unit cell oriented along the (0 1 1) direction (a). Graphical representation of the π-π stacking (2 3 2) and lamellar (0 1 1) peaks orientation with respect to the (0 1 1) vector (b). m-4TICO (c) and PBTZT-stat-BDTT-8:m-4TICO (d) GIWAXS pattern with in-plane (e) and out-of-plane (f) integration profiles. 5x5 µm AFM images of m-4TICO (f) and PBTZT-stat-BDTT-8:m-4TICO (g) films with domain size distribution and average value (inset).

Table S5. Crystallographic information of the main peaks observed by 2D-GIWAXS on m-4TICO and PBTZT-stat-BDTT-8:m-4TICO films. AFM domain size and domain purity are also shown.

Component	Peak	Orientation	q (nm^{-1})	d (nm)	FWHM (nm^{-1})	CCL (nm)	g	Domain Size (nm)	φ (%)
				NFA film					
m-4TICO	(0 1 1)	Out-of-plane	4.52	1.39	0.33	17.1	10.8	62.1	27.6
				Blend film					
m-4TICO	(0 1 1)	Out-of-Plane	4.25	1.48	0.59	9.6	14.9	68.5	14.0
PBTZT-stat-BDTT-8	(1 0 0)	In-plane	2.60	2.42	1.42	4.0	29.5	-	-
PBTZT-stat-BDTT-8	(0 1 0)	Out-of-plane	17.85	0.35	5.00	1.1	21.1	-	-

m-ITIC

m-ITIC 2D-GIWAXS pattern (Figure S11c) shows a couple of features in the π-π stacking region along q_z and other less intense peaks in the low angle region, both in-plane and out-of-plane. To verify whether the NFA arrangement in film is compatible to the phase existing in powder and single crystal, we have simulated the 2D-GIWAXS of the single crystal unit cell[5] (Le Bail refined) and oriented along the (1 1 1) direction (Figure S11a). Such direction is perpendicular to the lamellar (0 -1 1) peak and parallel with respect to π-π stacking features, (2 3 3) and (2 2 5). This is representative of a face-on orientation of the m-ITIC domains with respect to the substrate (Figure S11b). The good agreement between experimental and simulated GIWAXS confirms a face-on 2D brickwork packing with respect to the substrate. The feature located $q_z \sim 5$ nm^{-1} represents the (1 1 1) reflections but is not evident from the simulation because of its purely perpendicular orientation with respect to the substrate (region not accessible). As the m-ITIC lamellar (0 1 -1) feature is still evident from the PBTZT-stat-BDTT-8:m-ITIC GIWAXS (Figure S11d) and in-plane integration profile (Figure S11h), we assume that the NFA is maintaining its crystalline order in blend with a slightly relaxed lamellar (0 1 -1) and (2 2 5) π-π stacking periodicity (Table S6) compared to the pure NFA film.

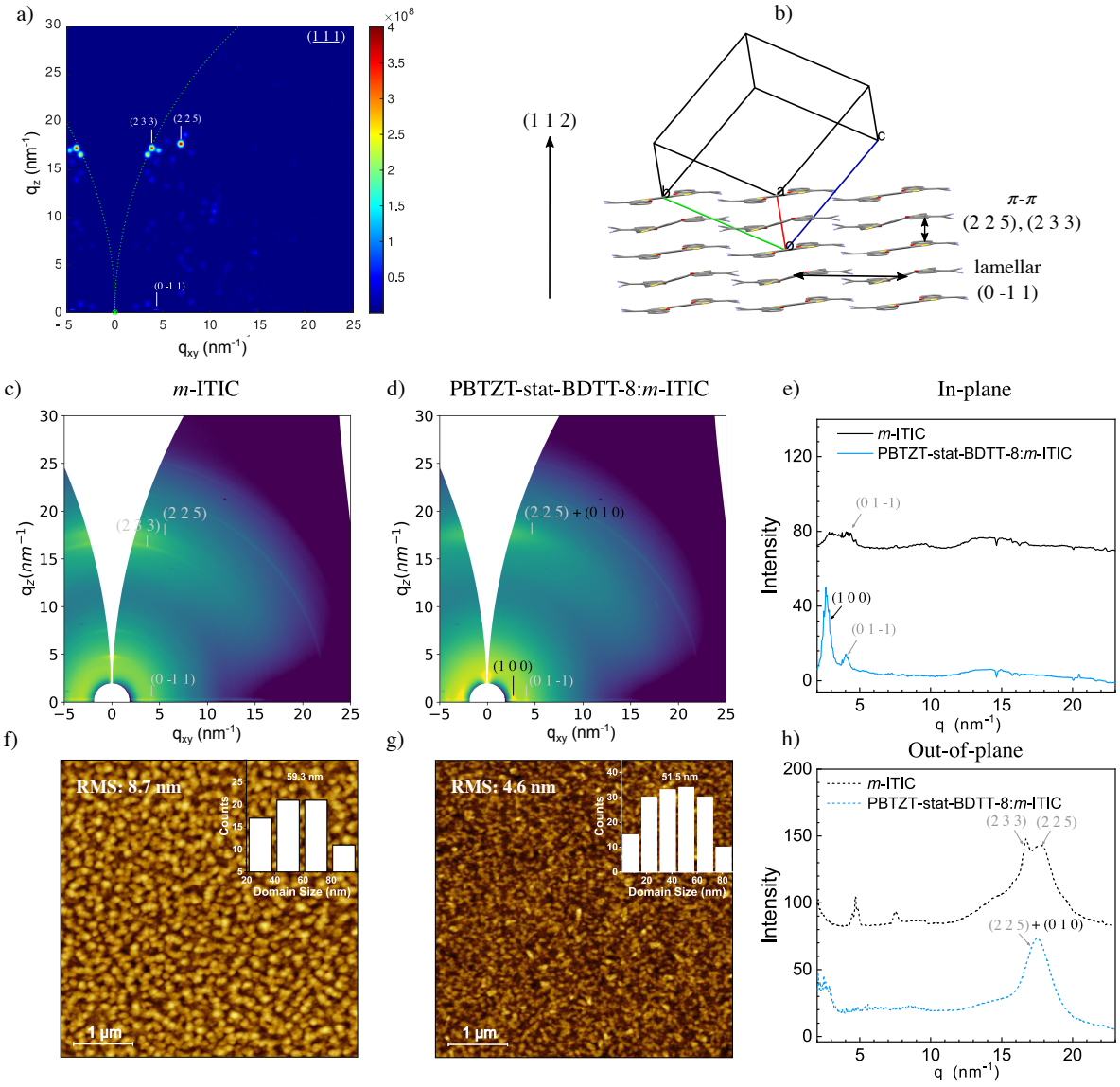

Figure S11. Simulated 2D-GIWAXS pattern of the m-ITIC unit cell oriented along the (1 1 1) direction (a). Graphical representation of the π-π stacking, (2 3 3) and (2 2 5), and lamellar (0 1 1) peaks orientation with respect to the (1 1 1) vector (b). m-ITIC (c) and PBTZT-stat-BDTT-8:m-ITIC (d) GIWAXS pattern with in-plane (e) and out-of-plane (h) integration profiles. 5x5 μm AFM images of m-ITIC (f) and PBTZT-stat-BDTT-8:m-ITIC (g) films with domain size distribution and average value (inset).

Table S6. Crystallographic information of the main peaks observed by 2D-GIWAXS on m-ITIC and PBTZT-stat-BDTT-8:m-ITIC films. AFM domain size and domain purity are also shown.

Component	Peak	Orientation	q (nm^{-1})	d (nm)	FWHM (nm^{-1})	CCL (nm)	g	Domain Size (nm)	φ (%)
			NFA film						
m-ITIC	(0 1 -1)	In-Plane	4.09	1.54	0.43	13.1	8.6	59.3	22.2
m-ITIC	(2 2 5)	Out-of-plane	17.75	0.35	2.41	2.3	14.7	-	-
			Blend film						
m-ITIC	(0 1 -1)	In-Plane	4.03	1.56	0.67	8.4	16.3	51.5	16.3
PBTZT-stat-BDTT-8	(1 0 0)	In-plane	2.67	2.35	0.55	10.2	18.1	-	-
PBTZT-stat-BDTT-8:m-ITIC	(0 1 0) + (2 2 5)	Out-of-plane	17.54	0.36	2.30	2.5	14.4	-	-

IDIC

IDIC 2D-GIWAXS pattern (Figure S12c) shows a couple of features in the π-π stacking region along q_z and multiple peaks in the low angle region among multiple directions. To verify whether the NFA arrangement in film is compatible to the phase existing in powder and single crystal, we have simulated the 2D-GIWAXS of the single crystal unit cell[5] (Le Bail refined) and oriented along the (2 2 3) direction (Figure S12a). Such direction is nearly perpendicular to the lamellar (0 1 0) peak and parallel with respect to the (2 1 3) π-π stacking feature, which is representative of a face-on orientation of the m-ITIC domains with respect to the substrate (Figure S12b). The partial agreement between experimental and simulated GIWAXS suggests a possible competition between two different polymorphs. The first one represented by the (0 1 0) and (2 1 3) features with a face-on 2D brickwork packing with respect to the substrate, while a second one identified by the (0 1 0)' and (2 1 3)' peaks. We hypothesise for the second polymorph to be still characterised by a face-on packing motif (2D or 3D) because of the presence of an intense out-of-plane (2 1 3)' π-π stacking feature and a (0 1 0)' lamellar peak developing along the in-plane direction. This second polymorph is becoming predominant in PBTZT-stat-BDTT-8:IDIC blend as visible from the GIWAXS data (Figure S12d), integration profiles (Figure S12e,h) and Table S7. As the IDIC lamellar (0 1 0)'

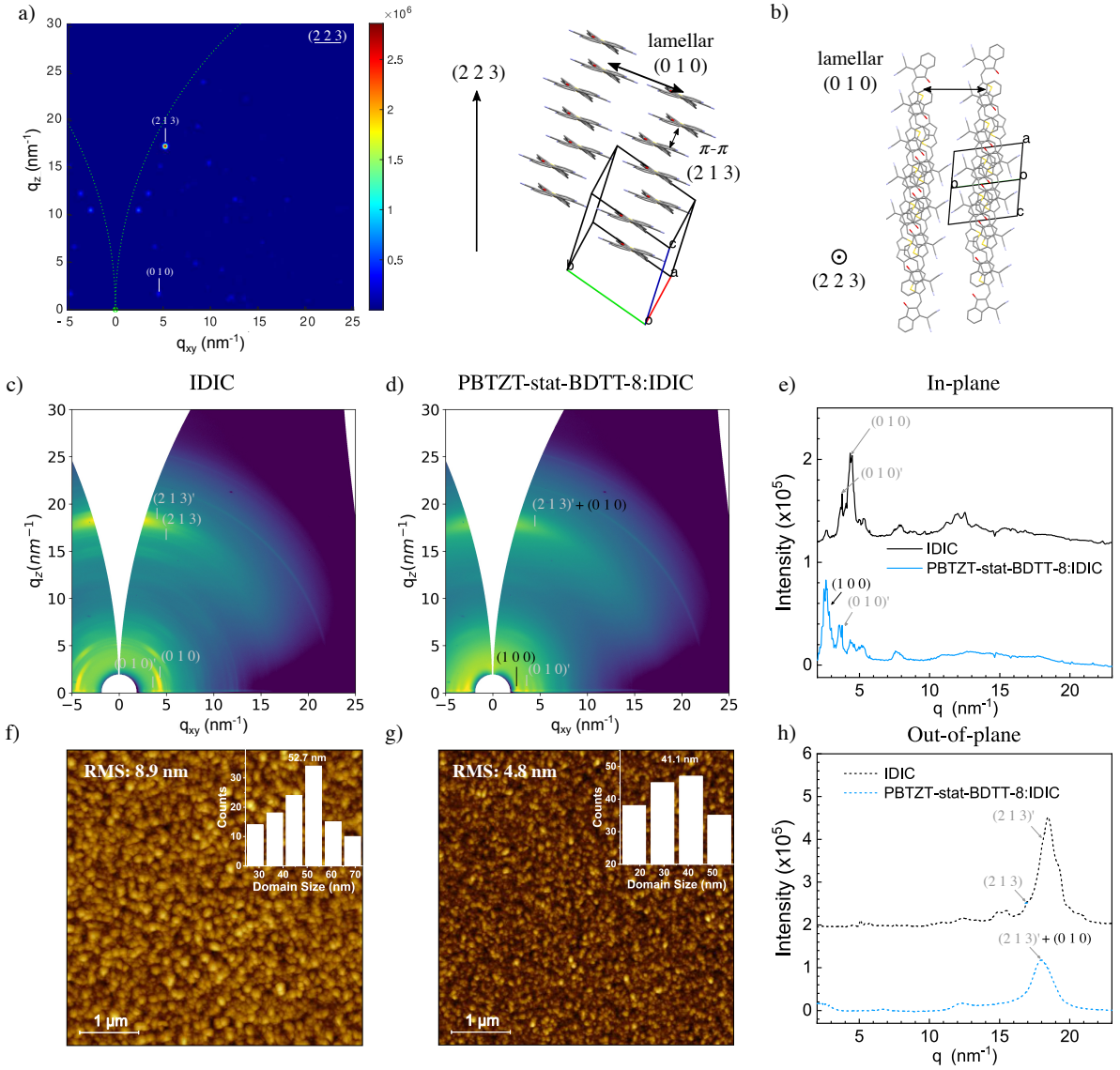

Figure S12. Simulated 2D-GIWAXS pattern of the IDIC unit cell (Le Bail refined) oriented along the (2 2 3) direction (a). Graphical representation of the (2 1 3) π-π stacking and (0 1 0) lamellar peaks orientation with respect to the (2 2 3) vector (b). IDIC (c) and PBTZT-stat-BDTT-8:IDIC (d) GIWAXS pattern with in-plane (e) and out-of-plane (h) integration profiles. 5x5 μm AFM images of IDIC (f) and PBTZT-stat-BDTT-8:IDIC (g) films with domain size distribution and average value (inset).

feature is still evident and distinguishable from the polymer, we assume that the NFA is still crystalline in the blend with a face-on 2D/3D crystal packing motif.

Table S7. Crystallographic information of the main peaks observed by 2D-GIWAXS on IDIC and PBTZT-stat-BDTT-8:IDIC films. AFM domain size and domain purity are also shown.

Component	Peak	Orientation	q (nm^{-1})	d (nm)	FWHM (nm^{-1})	CCL (nm)	g	Domain Size (nm)	φ (%)
			NFA film						
IDIC	(0 1 0)	In-Plane	4.32	1.45	0.26	21.7	9.8	52.7	41.2
IDIC	(2 1 3)	Out-of-plane	18.46	0.34	1.44	3.9	11.1	-	-
			Blend film						
IDIC	(0 1 0)'	In-Plane	3.60	1.74	0.54	10.5	15.4	41.1	25.5
PBTZT-stat-BDTT-8	(1 0 0)	In-plane	2.62	2.40	0.59	9.6	18.9	-	-
PBTZT-stat-BDTT-8:m-ITIC	(0 1 0) + (2 1 3)'	Out-of-plane	18.05	0.35	1.79	3.1	12.6	-	-

4TICO

4TICO 2D-GIWAXS pattern (Figure S13a) is characterised by a weak crystallinity as it only presents two main features, both featuring a lack of domain ordering along any specific direction. For this reason, it is not convenient to perform a side-by-side comparison with the single crystal structure.[5] However, a low angle (1 0 0) and a high angle (0 1 0) diffraction rings can still be distinguished (Figure S13a,b) and used for the evaluation of the NFA crystallinity in films (Table S8). As regards the PBTZT-stat-BDTT-8:4TICO blend, we could differentiate between the 4TICO and PBTZT-stat-BDTT-8 lamellar reflections since the latter is typically characterised by in-plane scattering in the low angle region (Figure 5). We therefore conclude that the NFA is weakly crystalline in the blend given the higher FWHM of the observed reflections with lack of texturing.

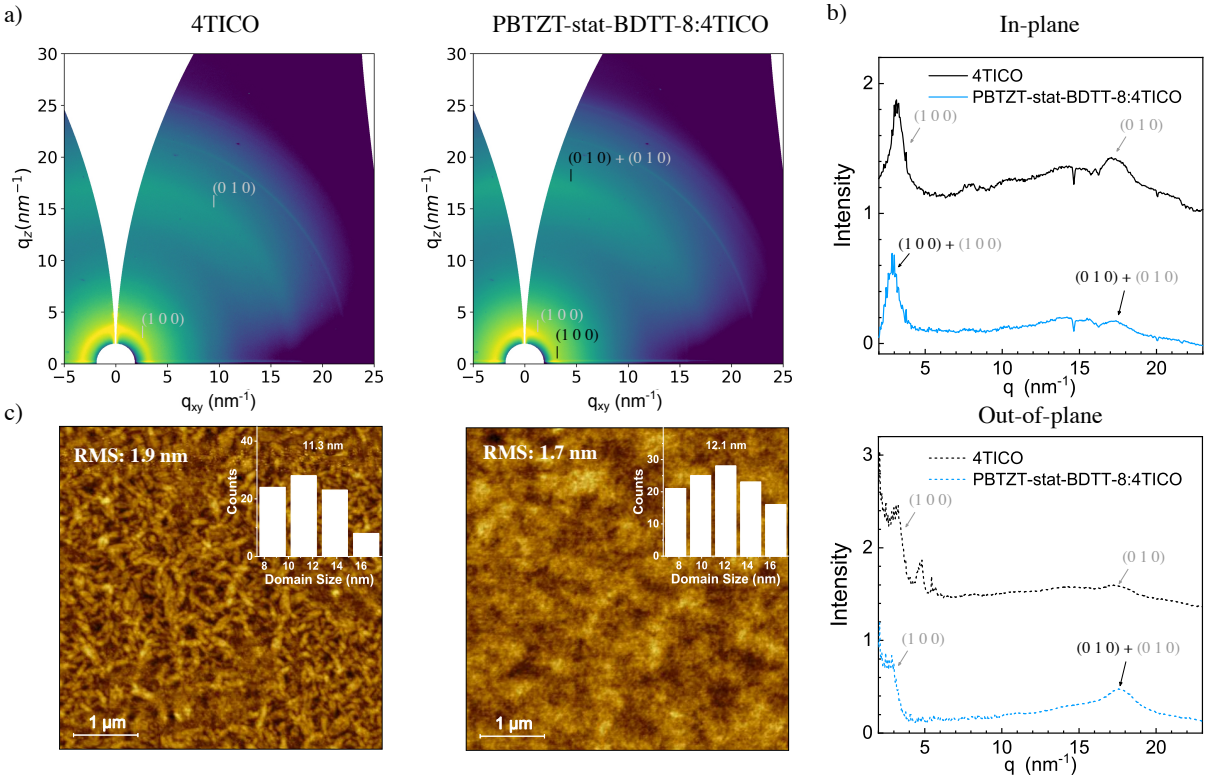

Figure S13. 4TICO and PBTZT-stat-BDTT-8:4TICO (a) GIWAXS patterns with in-plane and out-of-plane (b) integration profiles. 5x5 µm AFM images (c) of IDIC and PBTZT-stat-BDTT-8:IDIC films with domain size distribution and average value (inset).

Table S8. Crystallographic information of the main peaks observed by 2D-GIWAXS on 4TICO and PBTZT-stat-BDTT-8:4TICO films. AFM domain size and domain purity are also shown.

Component	Peak	Orientation	q (nm^{-1})	d (nm)	FWHM (nm^{-1})	CCL (nm)	g	Domain Size (nm)	φ (%)
			NFA film						
4TICO	(1 0 0)	In-Plane	3.20	1.96	0.89	6.3	21.0	11.3	56.2
4TICO	(0 1 0)	Out-of-plane	17.55	0.36	3.09	1.8	16.7	-	-
			Blend film						
4TICO	(1 0 0)	In-Plane	3.12	2.01	0.98	5.8	22.4	12.1	47.7
PBTZT-stat-BDTT-8	(1 0 0)	In-plane	2.77	2.27	0.64	8.8	19.2	-	-
PBTZT-stat-BDTT-8:4TICO	(0 1 0)	Out-of-plane	17.67	0.36	3.14	1.8	16.8	-	-

ITIC

ITIC 2D-GIWAXS pattern (Figure S14a) is characterised by a weak crystallinity as it only presents one main feature with a lack of domain ordering along any specific direction. For this reason, it is not convenient to perform a side-by-side comparison with the single crystal structure.[5] However, a low angle (1 0 0) diffraction ring can still be distinguished (Figure S14a,b) and used for the evaluation of the NFA crystallinity in films (Table S9). As regards the PBTZT-stat-BDTT-8:ITIC blend, we could differentiate between the ITIC and PBTZT-stat-BDTT-8 lamellar reflections since the two are characterised by a different in-plane lattice spacing (Table S9 and Figure S14). We therefore conclude that the NFA is poorly crystalline in the blend given the high FWHM of the observed reflections with lack of directionality.

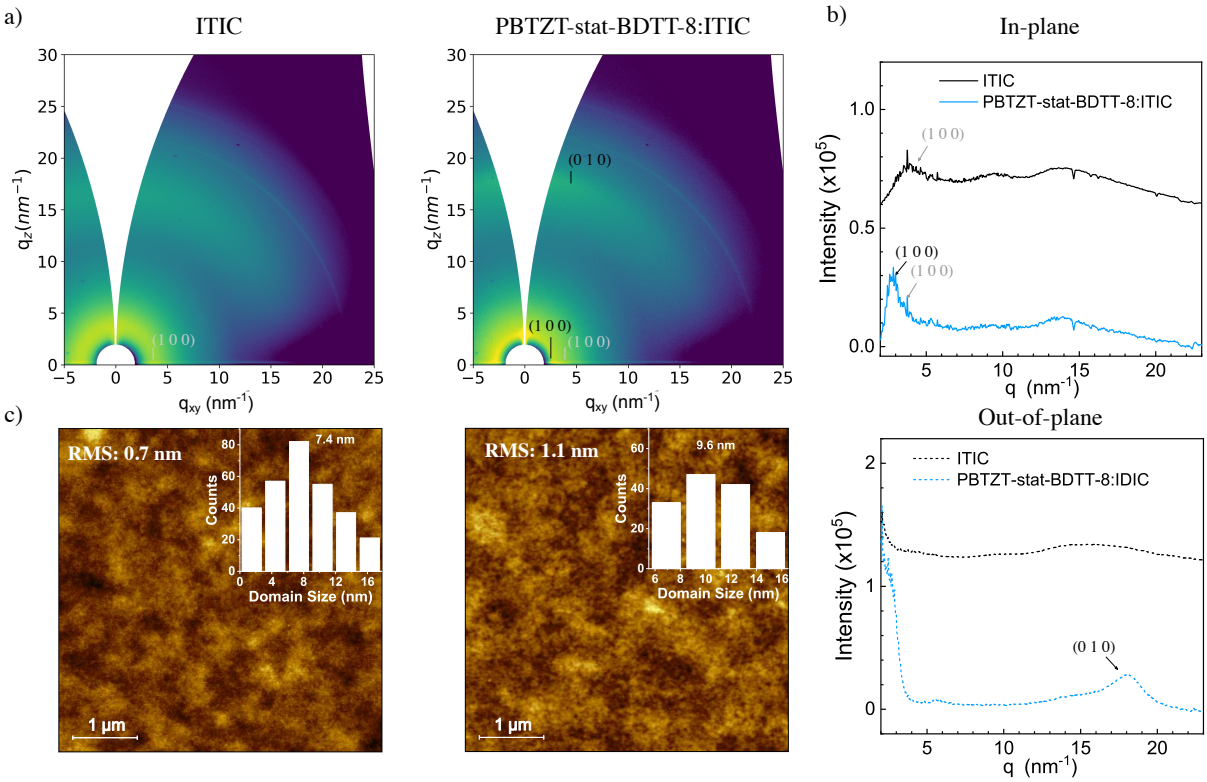

Figure S14. ITIC and PBTZT-stat-BDTT-8:ITIC (a) GIWAXS patterns with in-plane and out-of-plane (b) integration profiles. 5x5 µm AFM images (c) of ITIC and PBTZT-stat-BDTT-8:ITIC films with domain size distribution and average value (inset).

Table S9. Crystallographic information of the main peaks observed by 2D-GIWAXS on ITIC and PBTZT-stat-BDTT-8:ITIC films. AFM domain size and domain purity are also shown.

Component	Peak	Orientation	q (nm^{-1})	d (nm)	FWHM (nm^{-1})	CCL (nm)	g	Domain Size (nm)	φ (%)
NFA film									
ITIC	(1 0 0)	In-Plane	3.66	1.72	1.65	3.43	26.8	7.4	46.3
Blend film									
ITIC	(1 0 0)	In-Plane	3.57	1.76	0.99	5.7	21.0	9.6	59.4
PBTZT-stat-BDTT-8	(1 0 0)	In-plane	2.76	2.28	0.79	7.1	21.3	-	-
PBTZT-stat-BDTT-8:4TICO	(0 1 0)	Out-of-plane	18.09	0.35	2.44	2.3	14.7	-	-

4. AFM Watershed Analysis

IDIC

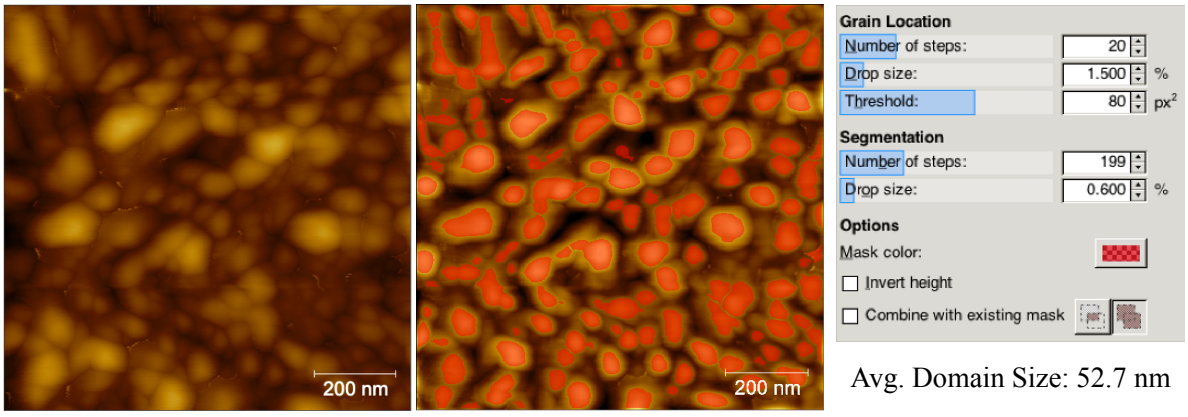

Avg. Domain Size: 52.7 nm

PBTZT-*stat*-BDTT-8:IDIC

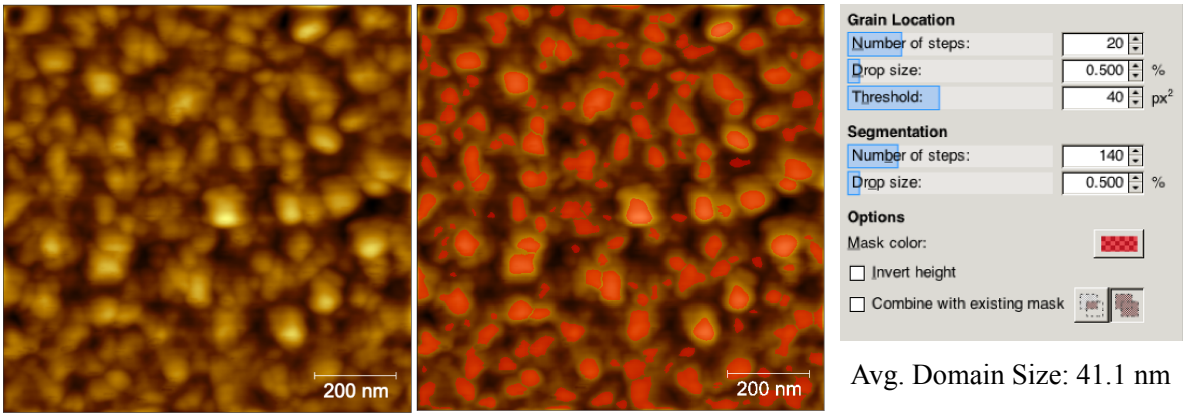

Avg. Domain Size: 41.1 nm

Figure S15. AFM images (1 µm x 1 µm) of IDIC and PBTZT-*stat*-BDTT-8:IDIC films with and without the mask used for the calculation of the average domain size by watershed algorithm. The input parameters and the result of the simulation are also shown.

m-ITIC

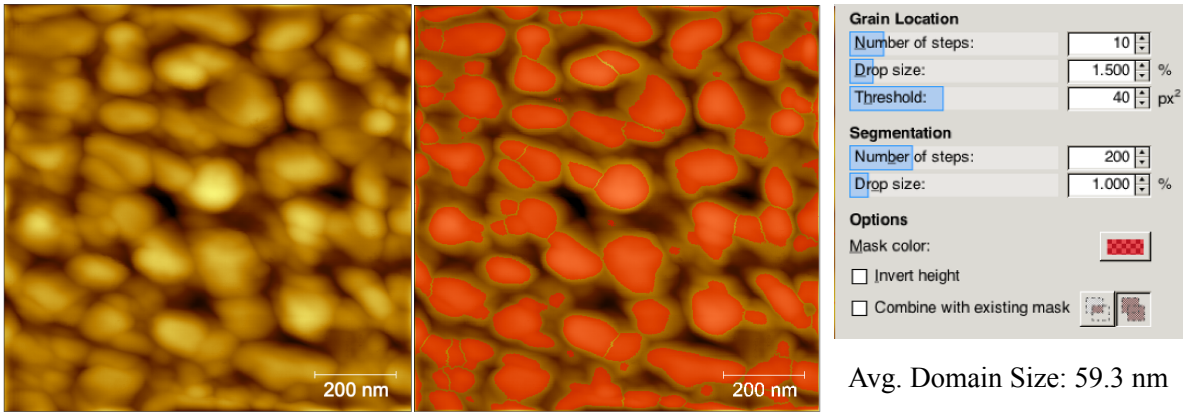

Avg. Domain Size: 59.3 nm

PBTZT-*stat*-BDTT-8:*m*-ITIC

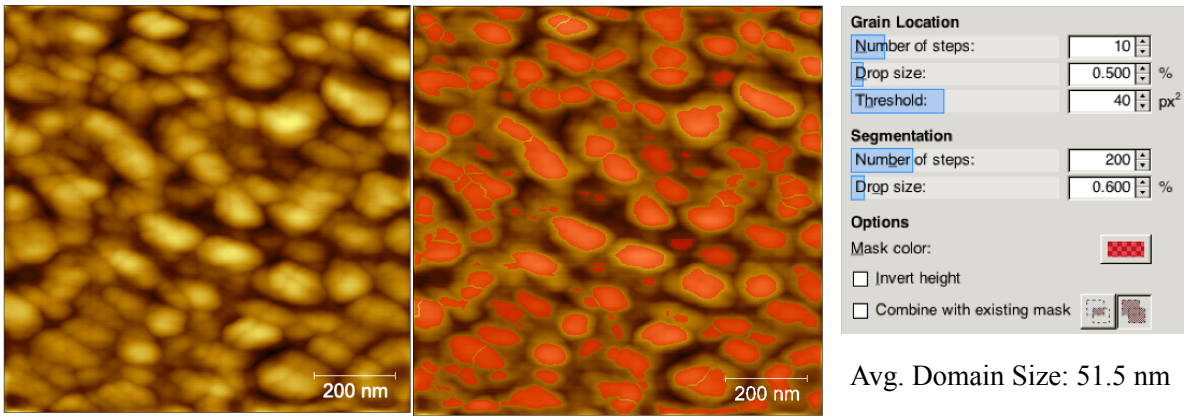

Avg. Domain Size: 51.5 nm

Figure S16. AFM images (1 µm x 1 µm) of *m*-ITIC and PBTZT-*stat*-BDTT-8:*m*-ITIC films with and without the mask used for the calculation of the average domain size by watershed algorithm. The input parameters and the result of the simulation are also shown.

o-IDTBR

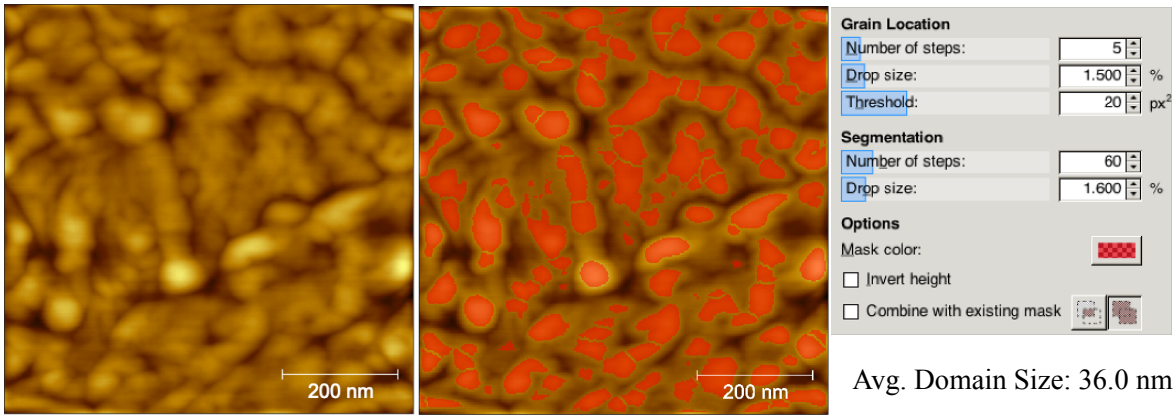

Avg. Domain Size: 36.0 nm

PBTZT-*stat*-BDTT-8:*o*-IDTBR

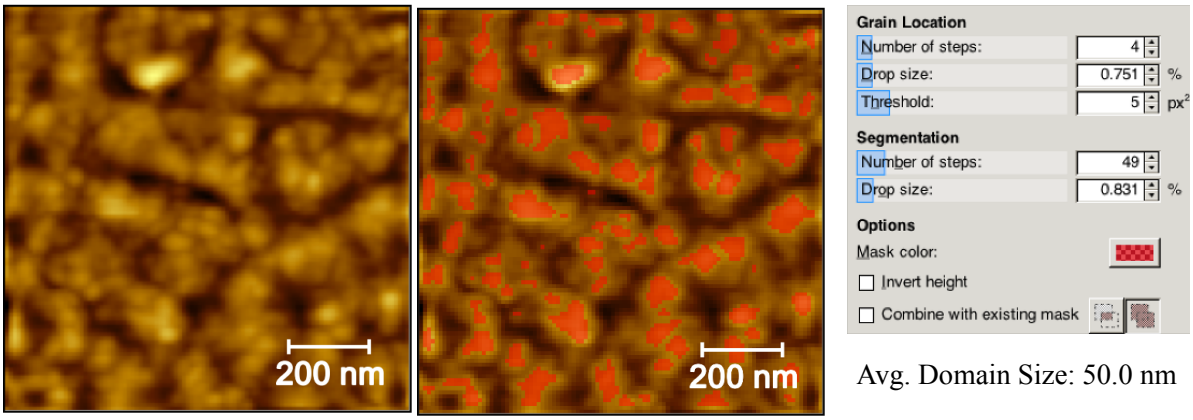

Avg. Domain Size: 50.0 nm

Figure S17. AFM images of *o*-IDTBR (0.6 µm x 0.6 µm) and PBTZT-*stat*-BDTT-8:*o*-IDTBR (1 µm x 1 µm) films with and without the mask used for the calculation of the average domain size by watershed algorithm. The input parameters and the result of the simulation are also shown.

m-4TICO

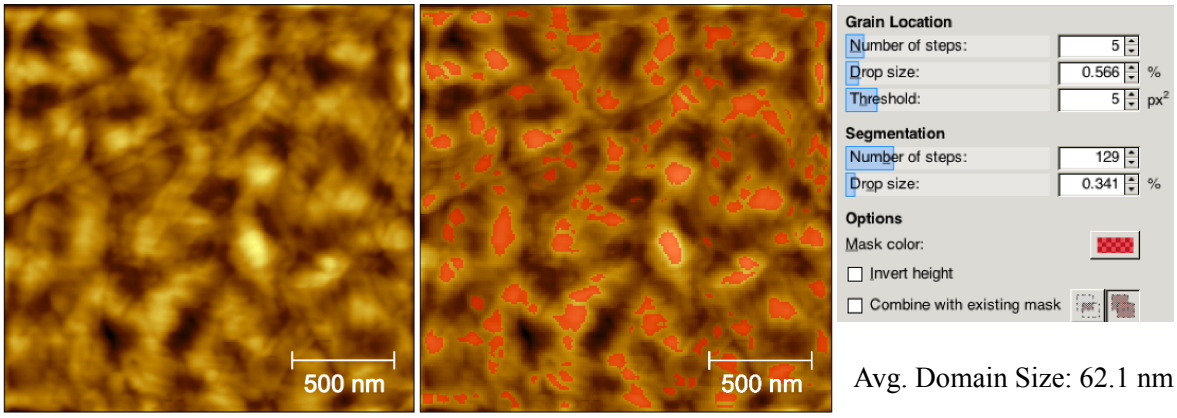

Avg. Domain Size: 62.1 nm

PBTZT-*stat*-BDTT-8:*m*-4TICO

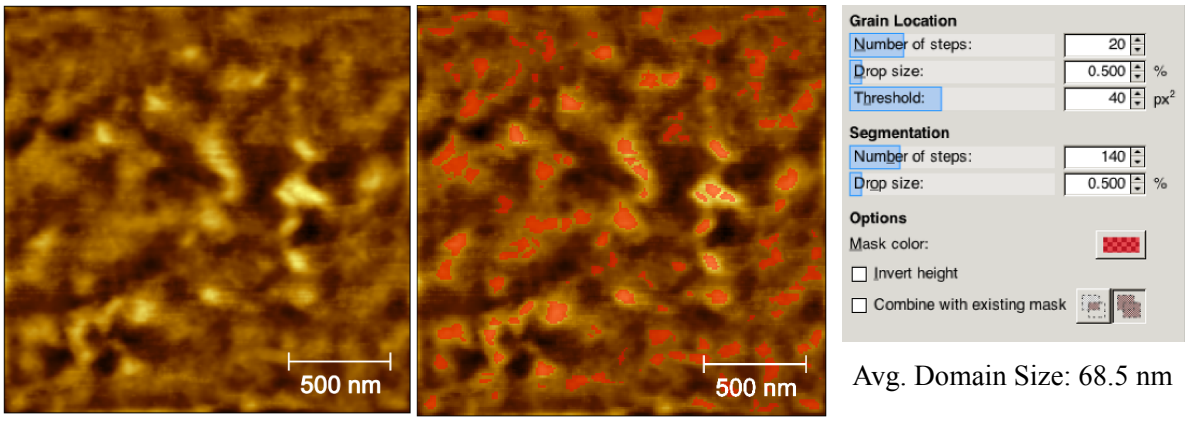

Avg. Domain Size: 68.5 nm

Figure S18. AFM images (2 µm x 2 µm) of *m*-4TICO and PBTZT-*stat*-BDTT-8:*m*-4TICO films with and without the mask used for the calculation of the average domain size by watershed algorithm. The input parameters and the result of the simulation are also shown.

ITIC

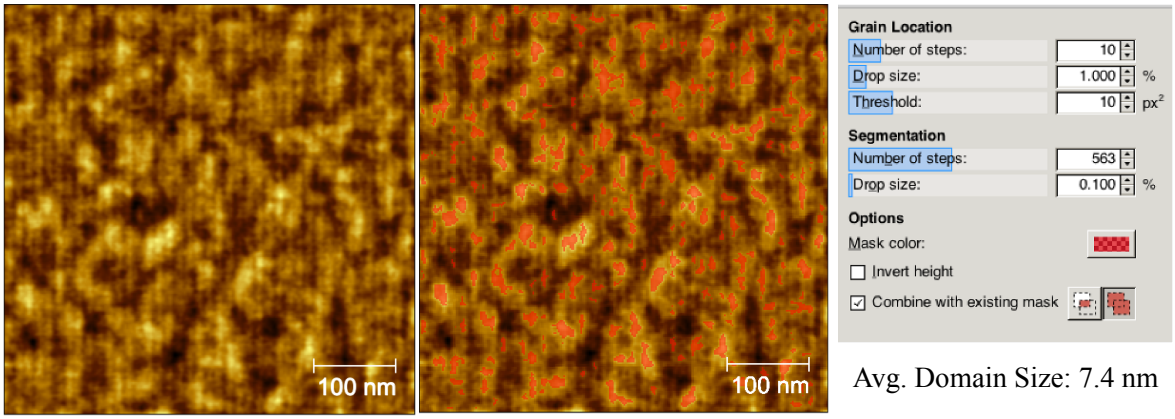

Avg. Domain Size: 7.4 nm

PBTZT-*stat*-BDTT-8:ITIC

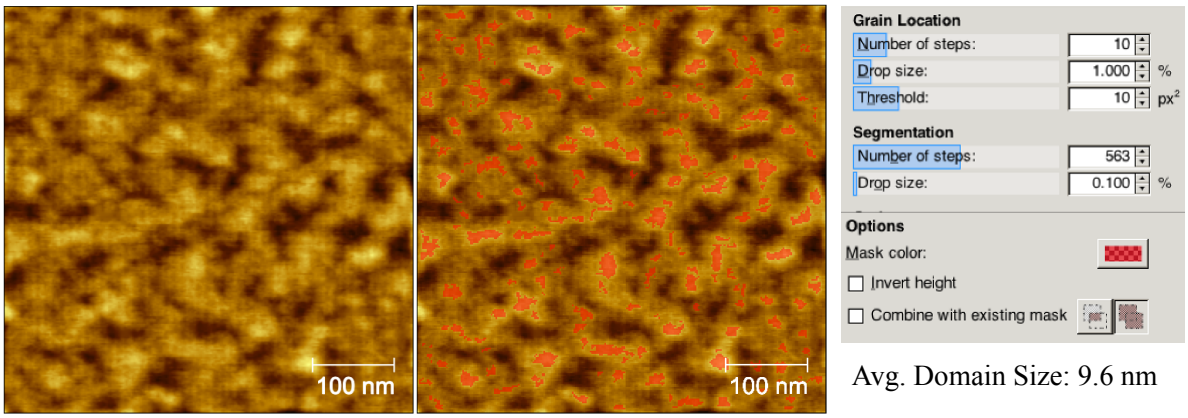

Avg. Domain Size: 9.6 nm

Figure S19. AFM images (0.5 µm x 0.5 µm) of ITIC and PBTZT-*stat*-BDTT-8:ITIC films with and without the mask used for the calculation of the average domain size by watershed algorithm. The input parameters and the result of the simulation are also shown.

4TICO

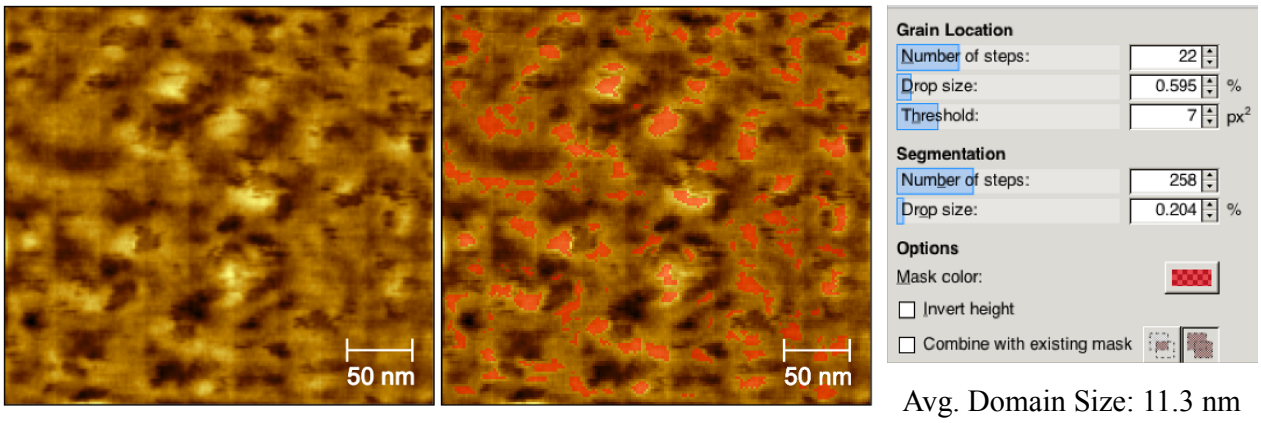

Avg. Domain Size: 11.3 nm

PBTZT-*stat*-BDTT-8:4TICO

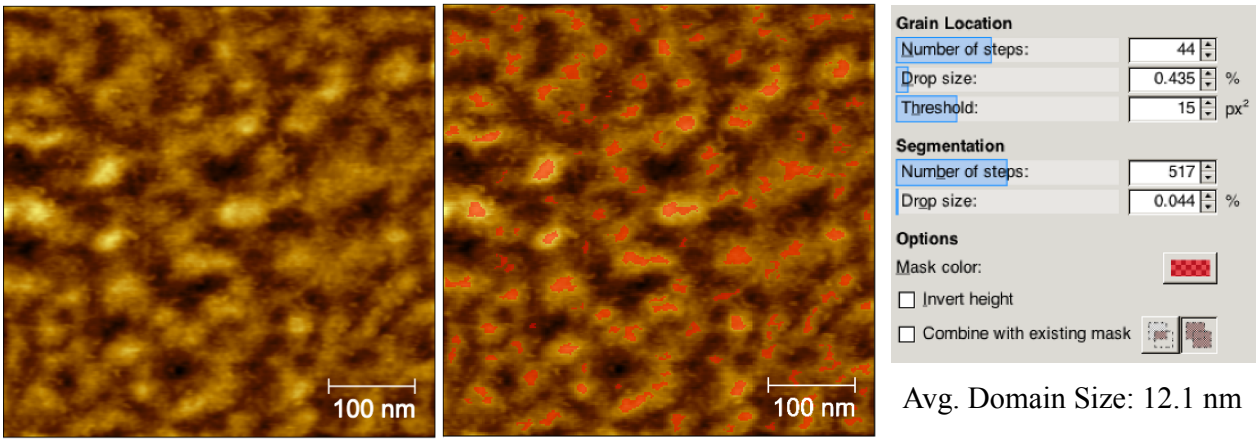

Avg. Domain Size: 12.1 nm

Figure S20. AFM images of 4TICO (0.3 µm x 0.3 µm) and PBTZT-*stat*-BDTT-8:4TICO (0.5 µm x 0.5 µm) films with and without the mask used for the calculation of the average domain size by watershed algorithm. The input parameters and the result of the simulation are also shown.

PBTZT-*stat*-BDTT-8:4TIC

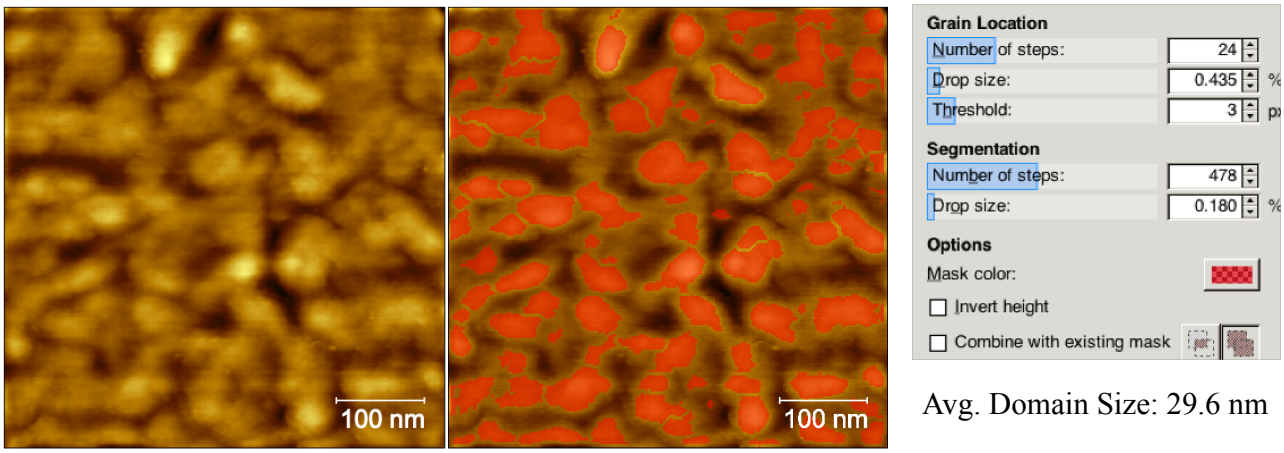

Avg. Domain Size: 29.6 nm

Figure S21. AFM images of PBTZT-*stat*-BDTT-8:4TIC (0.5 µm x 0.5 µm) films with and without the mask used for the calculation of the average domain size by watershed algorithm. The input parameters and the result of the simulation are also shown.

5. Electron Mobility by MIS-CELIV

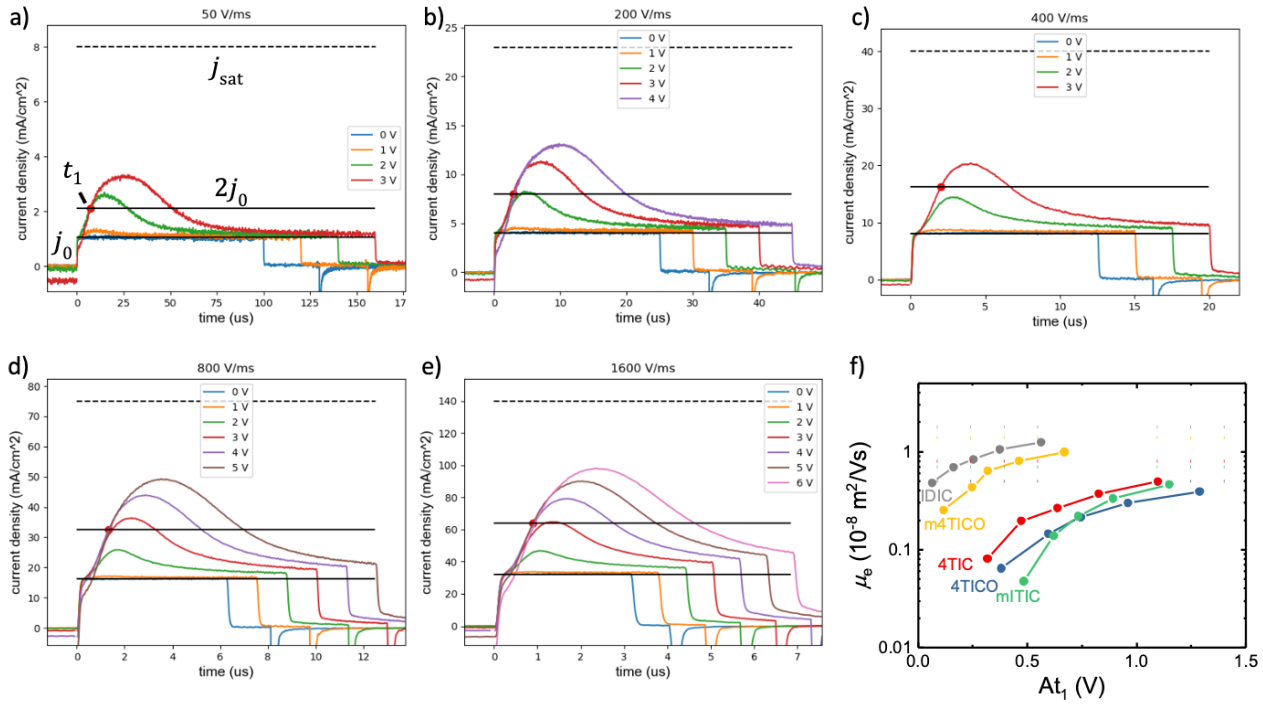

Figure S22 Typical MIS CELIV dataset taken for the 4TIC blend. The ramp rate *A* was varied between (a) 50 V/ms, (b) 200V/ms, (c) 400V/ms, (d) 800V/ms, and (e) 1600V/ms. (f) Extracted electron mobilities for the different blends in dependence of the ramp rate. Dashed lines indicated the estimated saturated mobility used in the main part. See text for further explanations.

Figure S15 shows representative example MIS-CELIV traces for PBTZT-stat-BDTT-8:4TIC. Different panels show measurements at different ramp rates and for each ramp rate the offset voltage is varied. The solid black lines indicate the displacement current density j_0 resulting from the geometric capacitance, and $2\times j_0$ used to determine time t_1 (red dot) in MIS-CELIV measurements. Finally, the saturated current density j_{sat} is estimated by the top dashed line. Due to imperfect properties of the insulating MgF_2 layer, hole injection from the metal back contact at high offset voltages cause a leakage current through the insulator and device. As a consequence the saturation current density j_{sat} cannot be reached and needs to be estimated. This was done by anticipating the typical saturation or flattening-out behaviour of MIS-CELIV curves[6]. Note that the extracted mobility values change little with the exact value of j_{sat}. With t_1, the mobility is calculated for all ramp rates and blends and plotted in fig. S15 (bottom right panel). In the presence of some injection barrier, the measured apparent mobility depends on the product of ramp rate A and t1. The measured mobility saturates and reaches its true value for large A×t1.6 The estimated saturated mobility is indicated with dashed lines in fig. S15 (bottom right panel).
With increasing annealing temperature, the blocking properties of MgF2 diminished and for some samples leakage currents prevented data analysis. Hence, the m-4TICO blend at 100°C, rather than 120°C, and the unannealed m-ITIC were analysed. However, we did not observe a notable change for other samples with annealing temperature. Hence, we can assume that the measured values are representative.

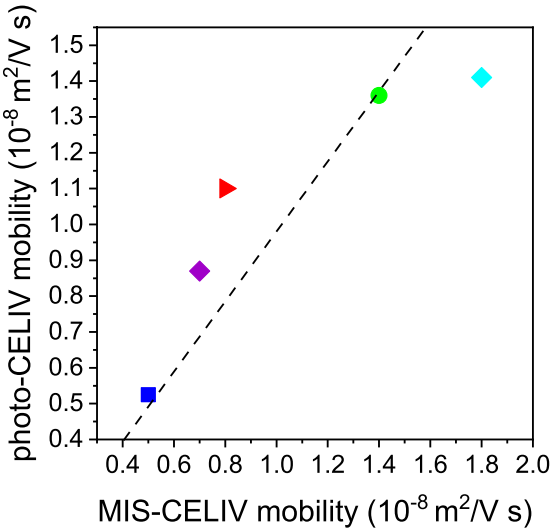

Figure S23. Photo-CELIV mobility compared to MIS-CELIV. A bisecting line is also plotted.

6. Active Layer Annealing Temperature and Dark J-V

Table S10. *Thermal annealing protocol used for each active layer.*

Active Layer	**Annealing Protocol**
PBTZT-stat-BDTT-8:o-IDTBR	5' at 100 °C
PBTZT-stat-BDTT-8:m-ITIC	5' at 100 °C + 5' at 120 °C + 3' at 140 °C
PBTZT-stat-BDTT-8:ITIC	5' at 100 °C + 5' at 120 °C + 3' at 140 °C
PBTZT-stat-BDTT-8:IDIC	5' at 100 °C + 5' at 120 °C
PBTZT-stat-BDTT-8:4TICO	5' at 100 °C + 5' at 120 °C + 3' at 140 °C
PBTZT-stat-BDTT-8:4TIC	5' at 100 °C + 5' at 120 °C + 3' at 140 °C
PBTZT-stat-BDTT-8:m-4TICO	5' at 100 °C + 5' at 120 °C

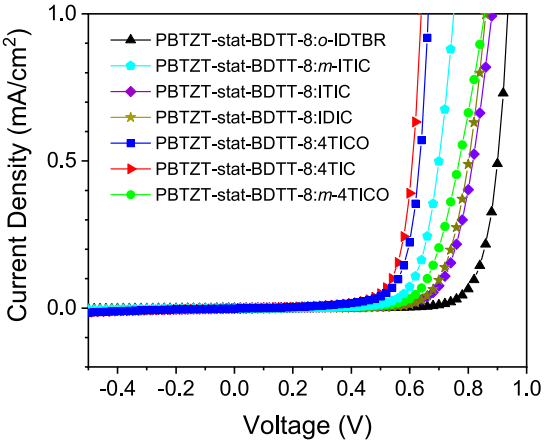

Figure S24. J-V characteristics measured in dark conditions.

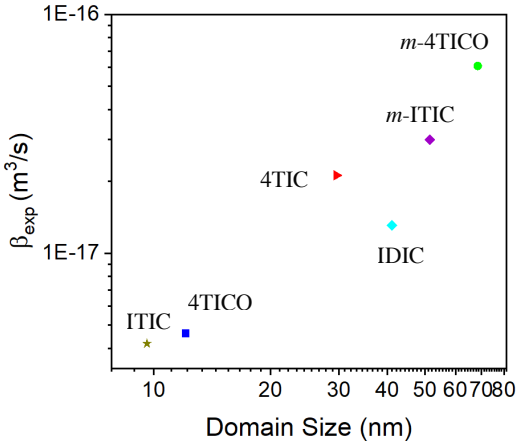

Figure S25. Plot showing the trend between the bimolecular recombination coefficient and the average domain size determined from AFM.

7. References

1. T. F. Schulze and T. W. Schmidt, *Energy & Environmental Science*, 2015, **8**, 103-125.
2. P. Mondelli, F. Silvestri, L. Ciammaruchi, E. Solano, E. Beltrán-Gracia, E. Barrena, M. Riede and G. Morse, *Journal of Materials Chemistry A*, 2021, **9**, 26917-26928.
3. X. Shi, L. Zuo, S. B. Jo, K. Gao, F. Lin, F. Liu and A. K. Y. Jen, *Chemistry of Materials*, 2017, **29**, 8369-8376.
4. J. B. Sherman, B. Purushothaman, S. R. Parkin, C. Kim, S. Collins, J. Anthony, T.-Q. Nguyen and M. L. Chabinyc, *Journal of Materials Chemistry A*, 2015, **3**, 9989-9998.
5. P. Mondelli, G. Boschetto, P. N. Horton, P. Tiwana, C.-K. Skylaris, S. J. Coles, M. Krompiec and G. Morse, *Materials Horizons*, 2020, **7**, 1062-1072.
6. O. J. Sandberg, M. Nyman, S. Dahlström, S. Sandén, B. Törngren, J.-H. Smått and R. Österbacka, *Applied Physics Letters*, 2017, **110**, 153504.